Soil to Society: Red-Mud-Derived Iron Oxide Electrocatalysts for Circular Nitrogen Upcycling via Green Ammonia production

Kanhai Kumar,[a] *and Karuna Kar Nanda* [a,c,e *]

[a]*Materials Research Centre, Indian Institute of Science, Bangalore-560012, India.*
[b]*Homi Bhabha National Institute, Anushaktinagar, Mumbai-400094, India.*
[c]*Institute of Physics, Bhubaneshwar-751005, India.*
*Email: nanda@iisc.ac.in

Table S1. Major utilization routes of the Red mud

Utilization Route	Processing / Modification	Main Application	Advantages	Limitations	References
Cement & construction materials	Mixing with cement clinker, geo-polymerization	Cement, bricks, concrete	Large-scale utilization, low cost	Heavy metal leaching, limited Fe utilization	1,2
Adsorbents for water treatment	Acid/alkali activation, calcination	Removal of phosphate, arsenic, dyes	High surface area, low cost	Regeneration difficulty	3,4
Catalyst / catalyst support	Calcination, metal doping	Catalysis, environmental reactions	Utilizes Fe, Al, Ti oxides	Often requires high temperature treatment	3,4
Metal recovery	Acid or alkali leaching, solvent extraction	Fe, Al, Ti, Sc recovery	Valuable metal extraction	Chemical waste generation	5–9
Magnetic materials	Reduction roasting + magnetic separation	Magnetic particles, ferrites	High Fe recovery	High energy consumption	5,6,9
Soil amendment	Neutralization and stabilization	Agriculture	Improves soil structure	Alkalinity and toxicity concerns	4,10
Pigments	Thermal treatment, purification	Iron oxide pigments	High Fe content useful	Color purity issues	4,10–12
Fe–polyphenol (Fe–O–C) framework	Mild acid extraction + tannic acid coordination	Functional Fe–polyphenol material	Closed-loop extraction, high Fe recovery	Lab scale (Early-stage concept)	This work

Table S2. Technologies/strategies developed for the Fe extraction from Red mud

Route	Leaching / Processing Conditions	Fe Recovery	Resource Recyclability	Product Type	Energy Demand	Circularity	References
Physical recovery Method							
Gravity & magnetic separation	Physical separation, ambient	49–70%	Yes	Iron-rich concentrate	Low	No	9,13–17
Flotation	Starch / oleate collectors, ambient	≤86%	Yes	Iron concentrate	Low	No	4,6,9,16,17
Hydro cyclone & Magnetic separation	Magnetic strength - 750 Gauss	60-70%	Yes	Hematite (Fe_2O_3 content)	High	Yes	7,9,16
Hydrometallurgy & chemical recovery Method							
H_2SO_4 leaching	2.8 M H_2SO_4, 50 °C, 45 min	~68%	Yes	Fe salts	Medium	No	15,18
HCl leaching	10 M HCl, 80 °C, 150 min	~95%	No	Fe salts	High	No	4,18,19
Oxalic acid leaching	1 M oxalic acid, UV, 75 °C, 2 h	>90%	No	Fe oxalates	Medium–High	No	9,18,19
Bioleaching	Fungal cultures	~87%	No	Fe ions	Low	No	14,20
Pyrometallurgy							
Carbothermal reduction	1050–1750 °C	High (~80-90%)	No#	Metallic Fe	Very High	No	9,13,21,22
Reduction Roasting	1100-1550 °C	~92%	No#	Metallic Fe	Very High	No	7,15,21,23
Alkaline carbonates additives	1000-1200 °C	~100%	No#	Metallic Fe	Very High	Yes	9,13,23,24
Plasma Smelting Technology	Graphite & fluxes with power of 35 kW DC	71%	No#	Metallic Fe	Very High	Yes	25
Microwave technology	1000 °C	88%	No#	Metallic Fe	Very High	Yes	9,21,26
Suspension magnetization roasting technology	520 °C	95.22 %	No#	Hematite and Goethite	Very High	Yes	13,27
Polyphenol-assisted cyclic extraction	Mild HCl + tannic acid, ambient	**85% (1st cycle) >99% (3 cycles)**	**Full acid & ligand reuse**	**Fe–polyphenol framework**	**Low**	**Closed loop**	**This Work**

#Resources like carbon dust, fluxes etc. utilized in Carbothermal reduction methods often consumed

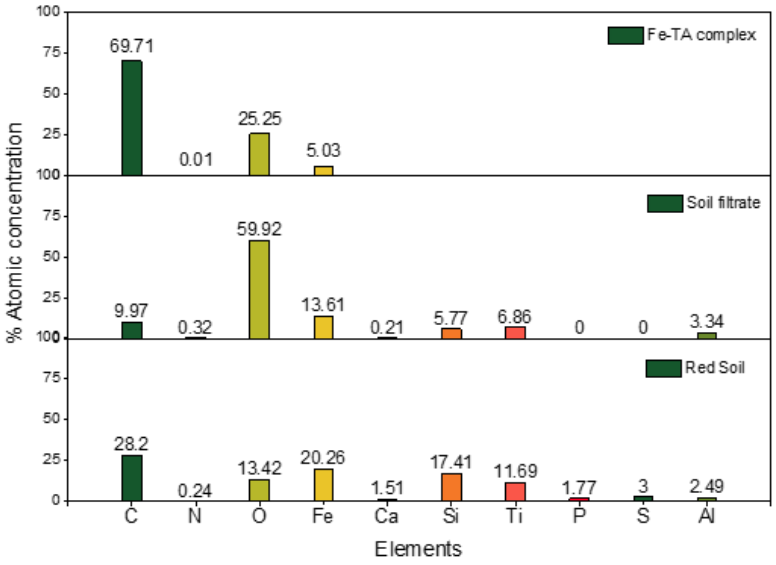

Figure S1. Quantification of XPS survey of Fe-TA complex (Black PPT), Soil filtrate and Red Soil (from top to down).

Table S3. FTIR Band Assignments for Tannic Acid (TA) and Iron–Tannic Acid Complex (Fe-TA)

Wavenumber (cm^{-1})	Notation	Assignment	Spectral Significance / Change upon Fe^{3+} Coordination
1696	ν(C=O)	Carbonyl stretching	Free galloyl ester C=O groups of tannic acid. Weakens upon Fe^{3+} complexation, indicating perturbation of the electronic environment around the carbonyl by the metal center.
1611	$\nu(C=C)_{Ar}$	Aromatic skeletal vibration	Aromatic ring C=C stretching confirming the polyphenol backbone. Relatively stable across TA and Fe-TA.
1539	$\nu(C–O)_{Ph}$	Phenolate asymmetric stretching	Primary coordination fingerprint. New or significantly enhanced band in Fe-TA corresponding to deprotonated phenolate groups coordinated to Fe^{3+}.
1442	δ(O–H) / ν(C–O)	Combined O–H bending / C–O stretching	Symmetric phenolate mode. Intensifies in Fe-TA. The $\Delta\nu \approx 97\ cm^{-1}$ separation from the 1539 cm^{-1} band is diagnostic of bidentate chelation (catecholate-type coordination).
1322	$\nu(C–O)_{Ph}$	Phenolic C–O stretching	Phenolic C–O stretch indicating the formation of the Fe–O(phenolate) interface.
1207 & 1154	ν(C–O–C)	Ester C–O–C / phenolic C–O stretching	Ester linkage and phenolic C–O stretches of TA's gallate arms. Broaden in Fe-TA, consistent with a distribution of slightly different Fe–O–C bond environments across multiple galloyl groups.
1009	ν(C–O–C)	Ester/ether C–O–C stretching	Sharp ester/ether band in TA that weakens and broadens in Fe-TA, suggesting Fe coordination indirectly perturbs the rigidity of gallate arm linkages.
910	$\delta(C–H)_{oop}$	Out-of-plane aromatic C–H bending	Out-of-plane C–H bending of the galloyl rings. Loses sharp character in Fe-TA due to reduced vibrational freedom upon metal-coordination.
849	ω(C=C)	Ring wagging / breathing mode	Aromatic ring breathing or wagging modes. Broadens in Fe-TA reflecting restricted ring motion in the metal-coordinated network.
768	$\delta(C–C)_{oop}$	Out-of-plane ring C–C deformation	Out-of-plane ring deformation mode. Merges into broader features in Fe-TA.
680	$\delta(C–C)_{ip}$	In-plane ring C–C deformation	In-plane ring deformation. Broadens in Fe-TA consistent with network rigidification.
643	ν(Fe–O)	Metal–oxygen stretching	Fe–O stretching mode. Intensification in Fe-TA confirms metal–oxygen coordination bond formation.

Abbreviations: ν, stretching; δ, bending; ω, wagging; oop, out-of-plane; ip, in-plane; Ph, phenolate; Ar, aromatic.

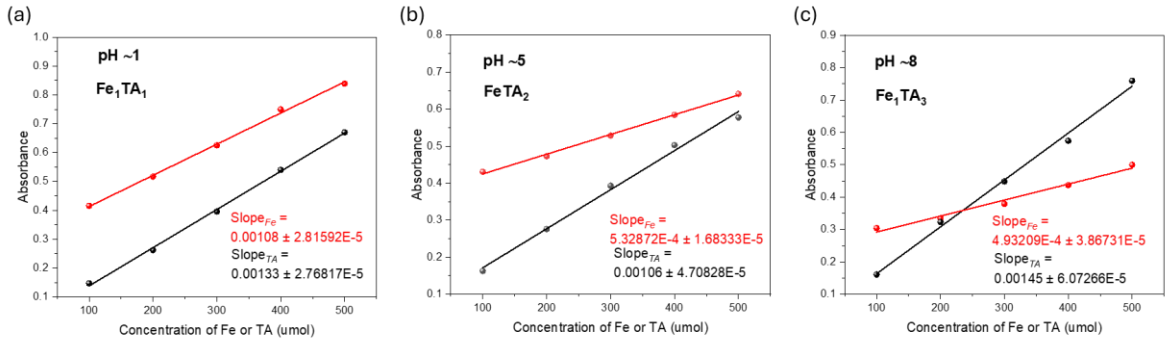

Figure S2. Slope-ratio UV–visible analysis for determining the coordination stoichiometry of Fe–tannic acid complexes at different pH values (pH 1, 5, and 8). The linear fitting slopes were used to determine the formation of FeTA, $FeTA_2$, and $FeTA_3$ species.

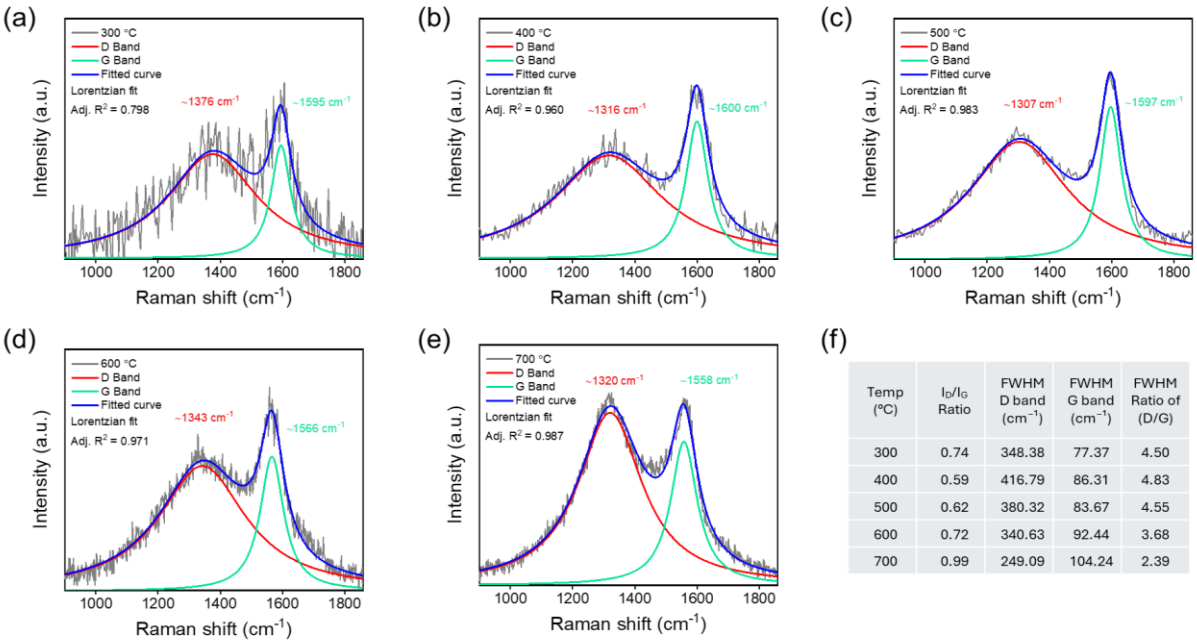

Temp (°C)	I_D/I_G Ratio	FWHM D band (cm^{-1})	FWHM G band (cm^{-1})	FWHM Ratio of (D/G)
300	0.74	348.38	77.37	4.50
400	0.59	416.79	86.31	4.83
500	0.62	380.32	83.67	4.55
600	0.72	340.63	92.44	3.68
700	0.99	249.09	104.24	2.39

Figure S3. Raman spectral deconvolution of Fe-TA precursor pyrolyzed at temperatures ranging from 300 to 700 °C. Each spectrum was deconvoluted into the D band (red, ~1307–1376 cm^{-1}, disordered carbon) and G band (green, ~1558–1600 cm^{-1}, graphitic sp^2 carbon), with cumulative fit in blue and raw data in grey. Key parameters are summarized in the inset table.

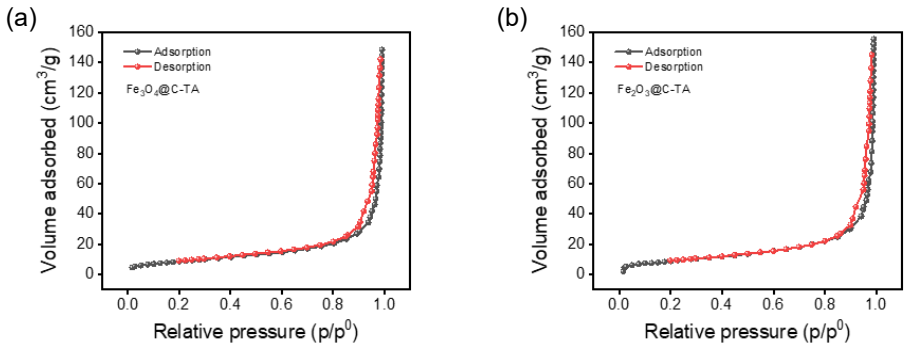

Figure S4. Nitrogen adsorption-desorption isotherm curves of (a) Fe_2O_3@C-TA, (b) Fe_3O_4@C-TA.

Table S4: BET measurement

Parameter	Unit	Fe_2O_3@C-TA	Fe_3O_4@C-TA
BET surface area (a_BET)	m^2/g	33.675	32.142
Monolayer volume (V_m)	cm^3 (STP)/g	7.737	7.385
BET constant (C)	—	46.52	55.596
Total pore volume	cm^3/g	0.2386	0.2253
Average pore diameter (BET)	nm	28.344	28.034
BJH pore volume (V_p)	cm^3/g	0.2306	0.209
BJH peak pore diameter	nm	1.1903	1.1903
BJH pore surface area (ap)	m^2/g	43.144	38.053
BJH average pore diameter	nm	21.377	21.968
BJH median pore diameter	nm	74.729	70.178
HK micropore volume (V_p)	cm^3/g	0.01586	0.01144
HK peak pore width	nm	1.0375	1.0375
HK micropore area (*ap*)	m^2/g	20.002	11.923
HK average pore width	nm	1.5861	1.9188
HK median pore width	nm	1.6039	2.1555

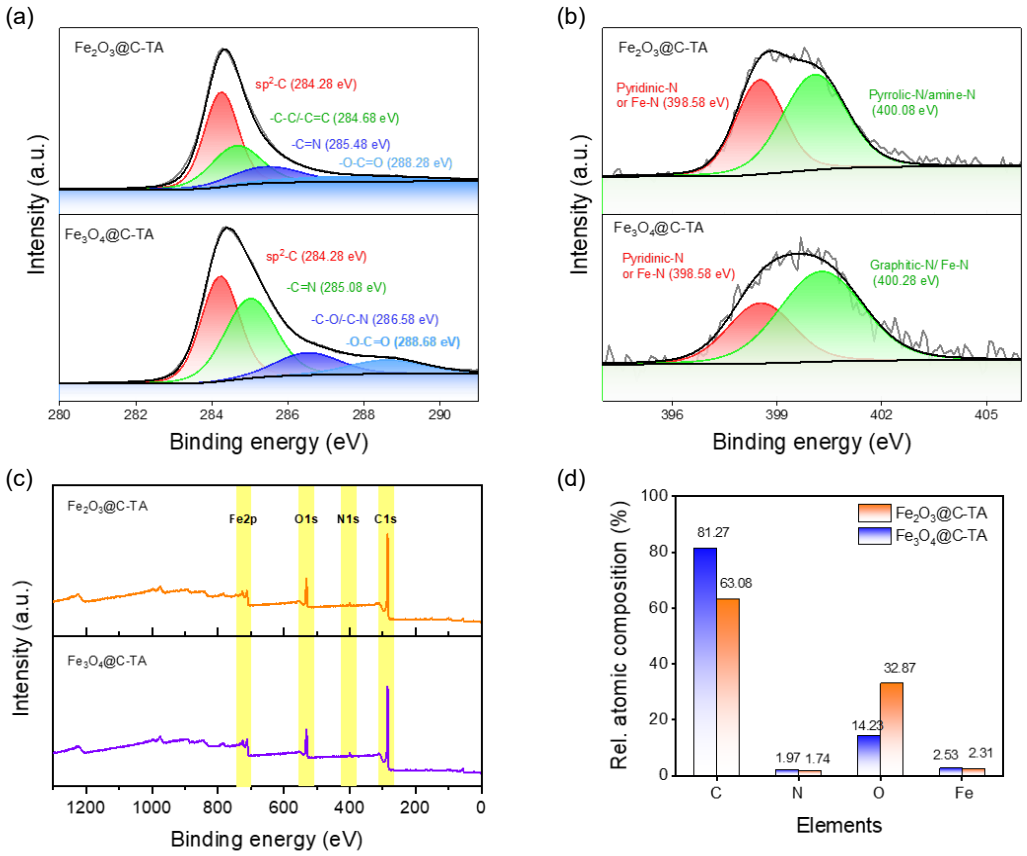

Figure S5. (a) High-resolution C 1s XPS spectra of both catalysts showing sp^2-C, C–N/C=N and O–C=O components. (b) High-resolution N 1s spectra of both catalysts displaying pyridinic-N/Fe–N, pyrrolic/amine-N and graphitic-N/Fe–N species. (c) XPS survey spectra confirming the presence of C, N, O and Fe elements. (d) Relative atomic composition derived from XPS analysis for both samples.

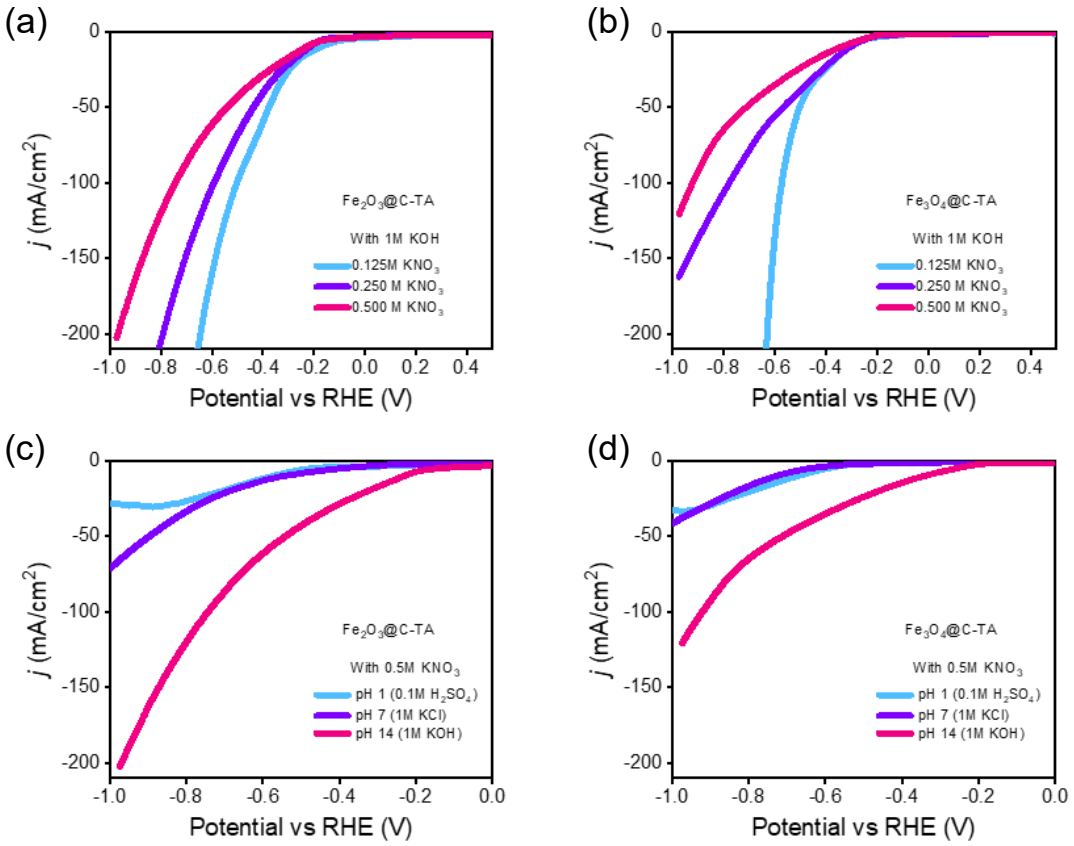

Figure S6. LSV curves in 1 M KOH containing varying KNO_3 concentrations (0.125 M, 0.25 M, and 0.5 M) with 1 M KOH as supporting electrolyte of (a) Fe_2O_3@C-TA and (b) Fe_3O_4@C-TA electrodes; LSV curves at varying pH conditions for (c) Fe_2O_3@C-TA and (d)Fe_3O_4@C-TA electrodes, demonstrating enhanced NO_3RR activity and steeper cathodic current response at pH 14 (1 M KOH).

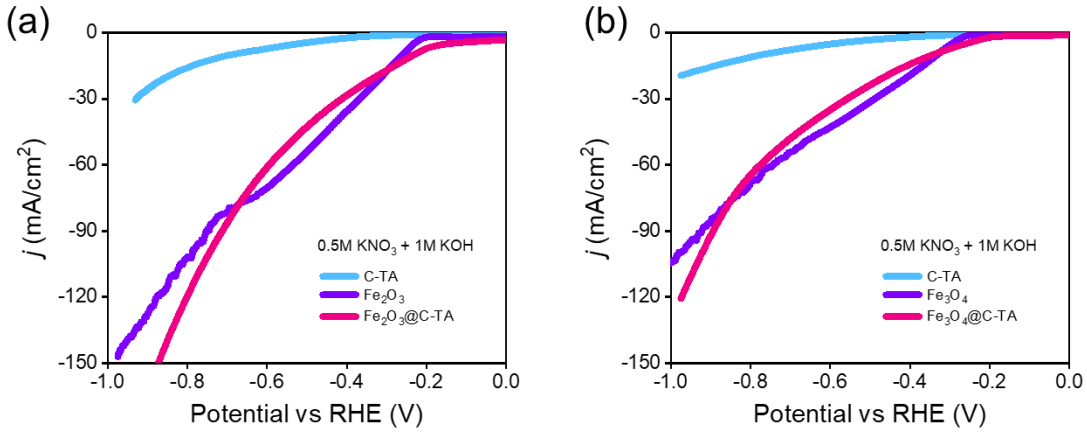

Figure S7. LSV curves in 0.5 M KNO_3 + 1 M KOH electrolyte of C-TA, Fe_2O_3, and Fe_2O_3@C-TA electrodes (a), and C-TA, Fe_3O_4, and Fe_3O_4@C-TA electrodes (b), where Fe_2O_3 or Fe_3O_4 and C-TA were individually studied to elucidate their respective contributions to the enhanced NO_3RR activity observed for the Fe_2O_3@C-TA or Fe_3O_4@C-TA composites respectively.

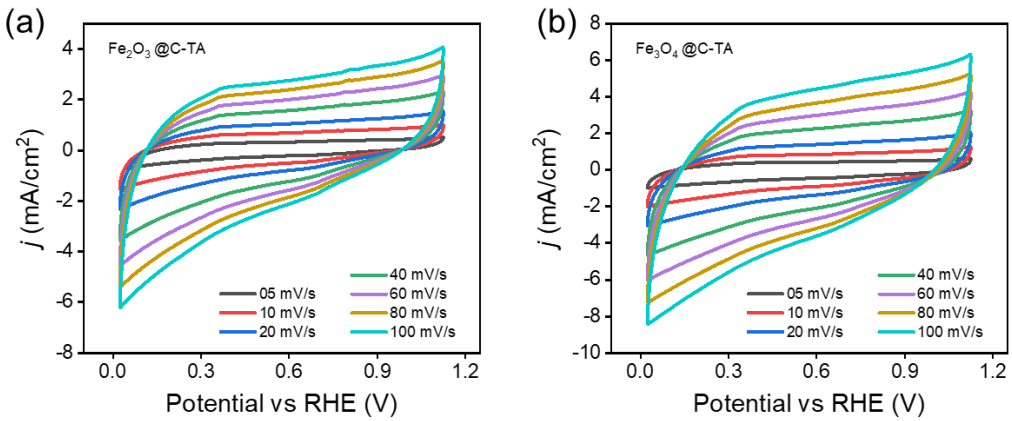

Figure S8. Cyclic voltammetry plots: (a) Fe_2O_3@C-TA, and (b) Fe_3O_4@C-TA in non-faradaic region for calculating C_{dl} and electrochemical surface area (ECSA) taking C_s = 50 µF/cm^2.

Table S5: Comparison of NO_3RR activity with recent reports

S. No.	Catalysts	Electrolytic medium	Faradaic efficiency (%)	Potential (V) vs. vs. RHE	Yield rate (mg h^{-1} cm^{-2})	Ref
1.	Fe-MoS_2	0.25M of $LiNO_3$ + 1M LiCl	~90	-0.85	9.75	28
2.	Co_3O_4/Co Nanosheets	0.1 M Na_2SO_4 + 1 mg mL^{-1} KNO_3	88.7	−0.8	4.43	29
3.	Co-CuO NAs	0.5 M PBS + 100 mgL^{-1}	96	-0.63	8.41	30
4.	Cu-WO_3	0.1 M KOH + 0.1 M NO_3^-	94	-0.63	2.13	31
5.	Ni_1Cu-SAA	200 ppm NO_3^- + 0.5M K_2SO_4	~100	-0.55	5.554	32
6.	BCN-Cu	0.1M KOH + 0.1M KNO_3	98.23	-0.5	1.900	33
7.	Pd/TiO_2	0.1M LiCl + 0.25M NO_3^-	92.1	-0.7	1.12	34
8.	Fe/Ni_2P	0.2M K_2SO_4 + 0.05M NO_3^-	94.3	-0.4	4.17	35
9.	FeN_2O_2	0.1M K_2SO_4 + 0.5M NO_3^-	92	-0.68	9.2	36
10.	Cu/Ni-NC	0.5 M Na_2SO_4 + 100 mgL^{-1} NO_3^-	97.28	-0.7	6.23	37
11.	S5-Co_3O4	0.1M Na_2SO_4 + 0.1M NO_3^-	89.9	-0.6	2.9614	38
12.	$Ru_{20}Ni_{80}$	0.5M K_2SO_4 + 0.1M NO_3^-	98.02	-0.35	8.65	39
13.	$CoTiO_3$@TiO_2/TM	0.1 M NaOH + 200 ppm KNO_3	94.66	-0.5	4.24 (-0.8V)	40
14.	F3CZNB	1M KOH + 0.1M NO_3^-	92.3	-0.6	5.67	41
15.	Au/Cu SAA	100 ppm NO_3^- + 0.5 M Na_2SO_4	99.69	-0.80	3.281	42
16.	Cu/Cu_2O NWAs	0.5m Na_2SO_4 + 200 ppm NO_3^-	95.8	-0.85	4.1633	43
17.	Cu_1Co_1HHTP	0.5 M Na_2SO_4 + 0.1M $NaNO_3$	96.4	-0.6	5.0983	44
18.	Co-Fe@Fe_2O_3	0.1 M Na_2SO_4 + 500 mgL^{-1} NO_3^-	85.2	-0.75	1.506	45
19.	Cu-N-C SACs	0.1M KOH + 0.1M NO_3^-	84.7	-1.0	4.5	46
20.	RuCu Das/NGA	0.1M KOH + 0.1M NO_3^-	95.7	-0.4	3.1	47
21.	NF/Ni_3N-Cu	1M KOH + 0.1M NO_3^-	98.7	-0.3	1.19	48
22.	$Pd_{63}Cu_{37}$ MSs	0.1M KOH + 0.01M NO_3^-	85	-0.25	6.1	49
23.	NiCu-SA	0.5M K_2SO_4 + 200 ppm NO_3^-	>90	-0.5	2.8	50
24.	NiCu-SAAs	1M KOH + 0.1M NO_3^-	95.4 ± 2.8	-0.6	11.4 ± 0.7	51
25.	Fe_2O_3@C-TA	0.5M KNO_3 + 1M KOH	93.67 ±1.67	-0.78	0.863±0.015 $mmolh^{-1}mg_{cat}^{-1}$ (7.352 ± 0.128 $mg{\cdot}h^{-1}{\cdot}cm^{-2}$)	This work
26.	Fe_3O_4@C-TA	0.5M KNO_3 + 1M KOH	58.66 ±1.05	-0.88	(2.938 ± 0.051 $mg{\cdot}h^{-1}{\cdot}cm^{-2}$)	This work

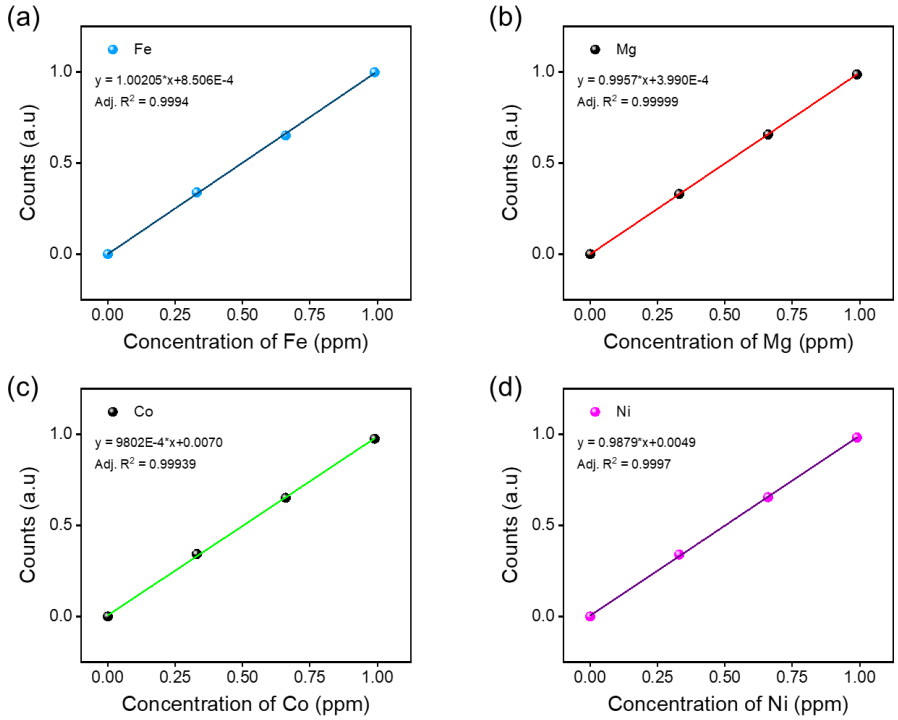

Figure S9. Calibration curve utilised for ICP-MS quantification of (a) Fe, (b) Mg, (c) Co and (d) Ni metals.

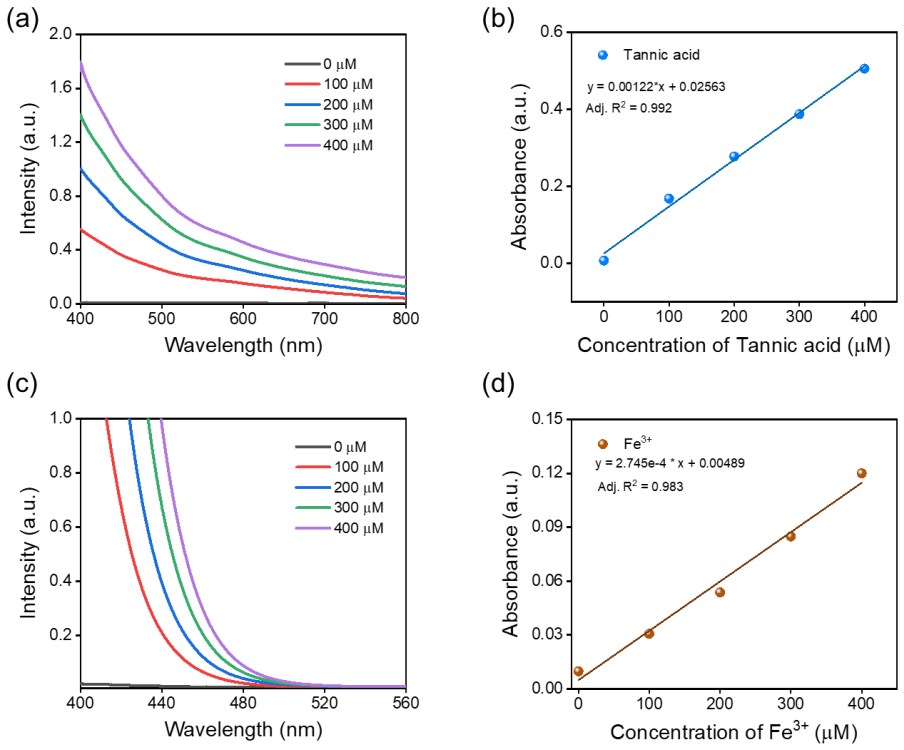

Figure S10. UV-Visible calibration curves used for quantification of (a) Tannic acid and (b) Fe^{3+}.

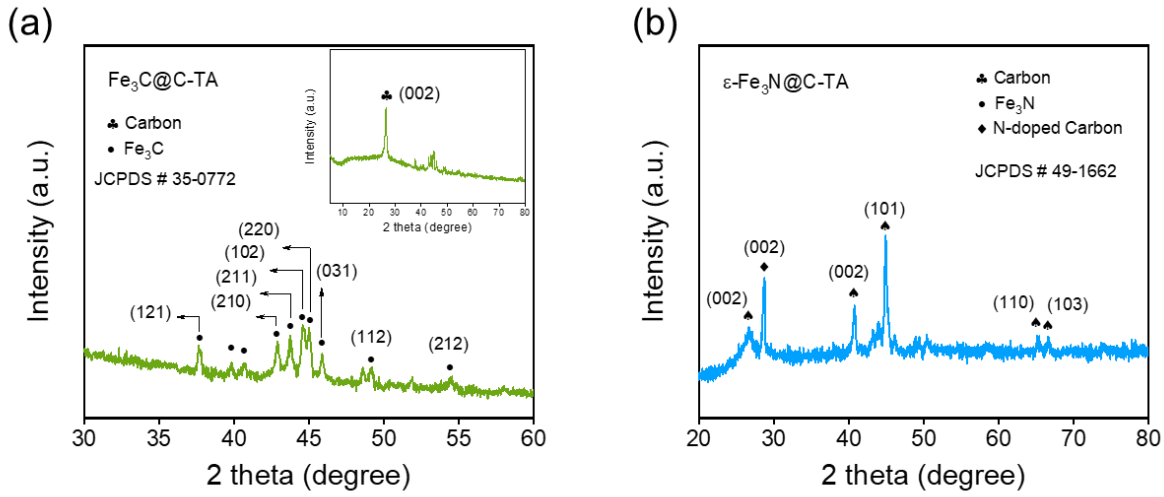

Figure S11. XRD spectra showing the phase-pure synthesis of (a) Fe_3C@C-TA and (b) Fe_3C@C-TA via catalyst portfolio.

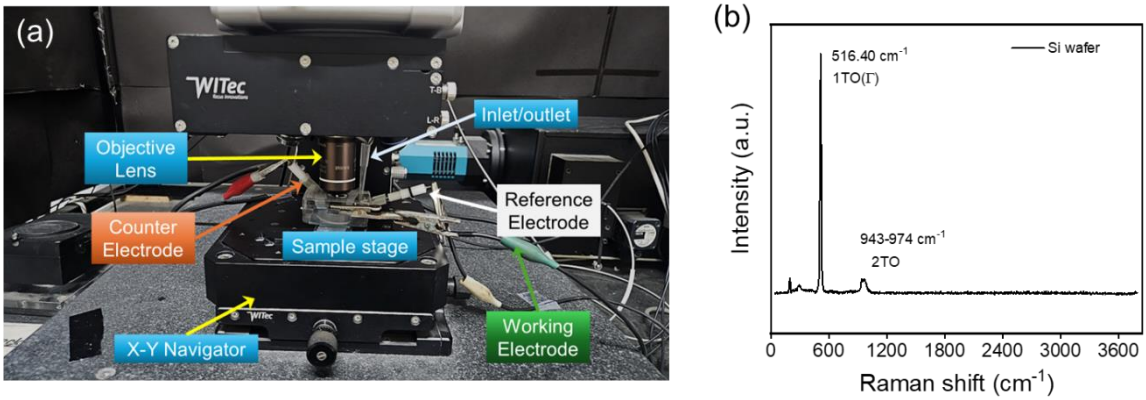

Figure S12. (a) Custom-designed *in situ* Raman set up and (b) The Si(100) wafer taken for Raman peak calibration; 1TO(Γ) peak at 516.40 cm^{-1} confirms accuracy and reference of spectrometer.

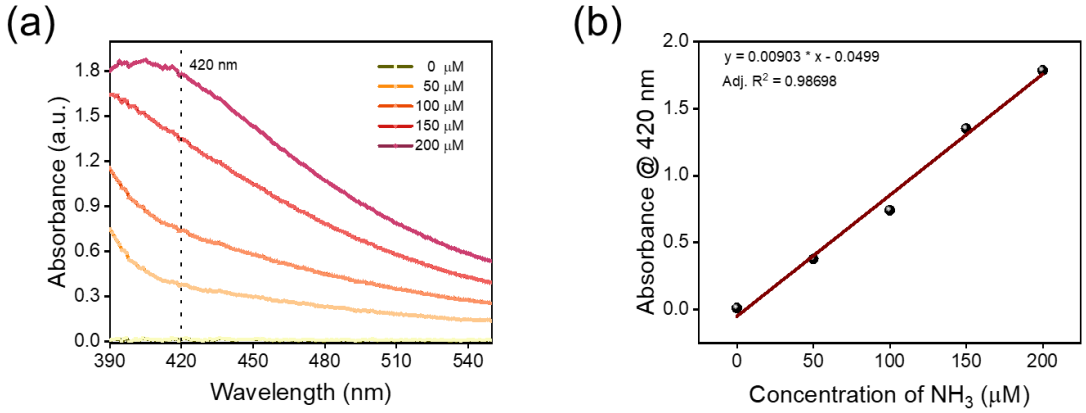

Figure S13. UV–visible spectrophotometric calibration curve of NH_4Cl for NH_3 quantification using Nessler's reagent.

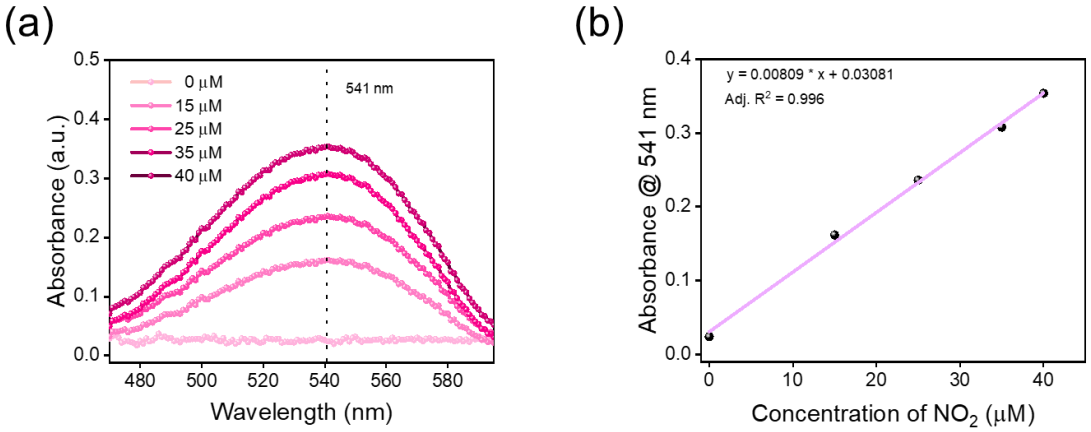

Figure S14. UV–visible spectrophotometric calibration curve of KNO_2 for NO_2^- quantification using Griess reagent.

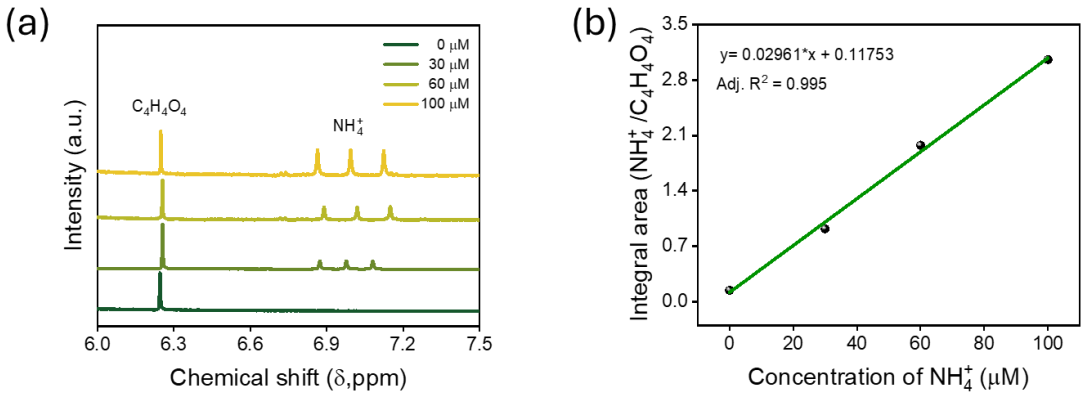

Figure S15. ^{1}H-NMR spectrophotometric calibration curve of NH_4Cl for NH_4^+ quantification.

References:

1 P. E. Tsakiridis, S. Agatzini-Leonardou and P. Oustadakis, *J. Hazard. Mater.*, 2004, **116**, 103–110.

2 L. Huang, C. Li, H. Wang, X. Li, Y. Qi and X. Zhu, *J. Phys. Conf. Ser.*, 2021, **2009**, 012021.

3 Z. Yang, L. Li and Y. Wang, *Molecules*, 2024, **29**, 974.

4 Z. Karimi and A. Rahbar-Kelishami, *Sci. Rep.*, 2023, **13**, 8527.

5 X. Pan, H. Wu, Z. Lv, H. Yu and G. Tu, *Sci. Total Environ.*, 2023, **904**, 166686.

6 D. Valeev, D. Zinoveev, A. Kondratiev, D. Lubyanoi and D. Pankratov, *Metals (Basel).*, 2020, **10**, 32.

7 S. Rai, M. T. Nimje, M. J. Chaddha, S. Modak, K. R. Rao and A. Agnihotri, *Miner. Eng.*, 2019, **134**, 222–231.

8 C. Laguna, F. González, C. García-Balboa, A. Ballester, M. L. Blázquez and J. A. Muñoz, *Miner. Eng.*, 2011, **24**, 10–18.

9 H. Kong, T. Zhou, X. Yang, Y. Gong, M. Zhang and H. Yang, *Energies*, 2022, **15**, 3830.

10 J. Li, X. Li, M. Fischel, X. Lin, S. Zhou, L. Zhang, L. Wang and J. Yan, *Toxics*, 2024, **12**, 347.

11 Y. Li, J. Wang, X. Wang, B. Wang and Z. Luan, *Phys. C Supercond. its Appl.*, 2011, **471**, 91–96.

12 J. Carneiro, D. M. Tobaldi, M. N. Capela, R. M. Novais, M. P. Seabra and J. A. Labrincha, *Waste Manag.*, 2018, **80**, 371–378.

13 S. Yuan, X. Liu, P. Gao and Y. Han, *J. Hazard. Mater.*, 2020, **394**, 122579.

14 T. C. Eisele and K. L. Gabby, *Miner. Process. Extr. Metall. Rev.*, 2014, **35**, 75–105.

15 T. Chun, D. Li, Z. Di, H. Long, L. Tang, F. Li and Y. Li, *J. South. African Inst. Min. Metall.*, 2017, **117**, 361–364.

16 L. Jiang, P. Liu, X. Yang, Y. Zhang and F. Li, *Miner. Eng.*, 2019, **131**, 124–130.

17 Y. Huang, G. Han, J. Liu and W. Wang, *J. Hazard. Mater.*, 2016, **301**, 46–55.

18 Y. Yang, X. Wang, M. Wang, H. Wang and P. Xian, *Int. J. Miner. Process.*, 2016, **157**, 145–151.

19 Y. Yang, X. Wang, M. Wang, H. Wang and P. Xian, *Hydrometallurgy*, 2015, **157**, 239–245.

20 N. Papassiopi, K. Vaxevanidou and I. Paspaliaris, *Miner. Eng.*, 2010, **23**, 25–31.

21 S. Agrawal, V. Rayapudi and N. Dhawan, *Miner. Eng.*, 2019, **132**, 202–210.

22 J. Zhao, L. Liu, Y. Yang, D. Liu, X. Peng, S. Liang and L. Jiang, *ACS Sustain. Chem. Eng.*, 2023, **11**, 2468–2475.

23 G. Ning, B. Zhang, C. Liu, S. Li, Y. Ye and M. Jiang, *Minerals*, 2018, **8**, 102.

24 D. Zinoveev, P. Grudinsky, A. Zakunov, A. Semenov, M. Panova, D. Valeev, A. Kondratiev, V. Dyubanov and A. Petelin, *Metals (Basel).*, 2019, **9**, 1313.

25 K. Jayasankar, P. K. Ray, A. K. Chaubey, A. Padhi, B. K. Satapathy and P. S. Mukherjee, *Int. J. Miner. Metall. Mater.*, 2012, **19**, 679–684.

26 W. L. Liang, Y. C. Zhang, Y. C. Li, Y. Q. Chang and M. R. Gao, *J. Am. Chem. Soc.*, 2025, **147**, 37223–37230.

27 J. Yu, Y. Li, Y. Lv, Y. Han and P. Gao, *Miner. Eng.*, 2022, **178**, 107394.

28 X. L. Junyang Ding, Xianghua Hou, Yuan Qiu, Shusheng Zhang, Qian Liu, Jun Luo, *Inorg. Chem. Commun.*,

2023, **151**, 110621.

29 F. Zhao, G. Hai, X. Li, Z. Jiang and H. Wang, *Chem. Eng. J.*, 2023, **461**, 141960.

30 Z. Li, Y. Li, C. Song, L. Fang and F. Yin, 2025, **8**, 2598–2606.

31 M. Wu, S. Li, K. Wei, H. Hu, Y. Song, Z. Zheng, H. Li and F. Gao, *Inorg. Chem. Front.*, 2025, **12**, 6631–6639.

32 J. Cai, Y. Wei, A. Cao, J. Huang, Z. Jiang, S. Lu and S. Q. Zang, *Appl. Catal. B Environ.*, 2022, **316**, 121683.

33 X. Zhao, X. Jia, Y. He, H. Zhang, X. Zhou, H. Zhang, S. Zhang, Y. Dong, X. Hu, A. V. Kuklin, G. V. Baryshnikov, H. Ågren and G. Hu, *Appl. Mater. Today*, 2021, **25**, 101206.

34 Y. Guo, R. Zhang, S. Zhang, Y. Zhao, Q. Yang, Z. Huang, B. Dong and C. Zhi, *Energy Environ. Sci.*, 2021, **14**, 3938–3944.

35 R. Zhang, Y. Guo, S. Zhang, D. Chen, Y. Zhao, Z. Huang, L. Ma, P. Li, Q. Yang, G. Liang and C. Zhi, *Adv. Energy Mater.*, 2022, **12**, 2103872.

36 W. Zhang, H. Dong, L. Zhou, H. Xu, H. Wang, X. Yan, Y. Jiang, J. Zhang and Z. Gu, *Appl. Catal. B Environ.*, 2022, **317**, 121750.

37 Yunlong Wang, H. Yin, X. Z. Feng Dong, Y. Qu, L. Wang, Y. Peng, D. Wang, * Wei Fang and Junhua Li*, *Small*, 2023, **19**, 2207695.

38 Z. Niu, S. Fan, X. Li, J. Yang, J. Wang, Y. Tao and G. Chen, *Chem. Eng. J.*, 2023, **451**, 138890.

39 Y. Xiong, M. Sun, S. Wang, Y. Wang, J. Zhou and F. Hao, 2025, **35**, 2420153.

40 Y. Wang, W. Zhang, W. Wen, X. Yu, Y. Du, K. Ni, Y. Zhu and M. Zhu, *Adv. Funct. Mater.*, 2023, **33**, 2302651.

41 L. Zhou, D. Feng, Z. Li, Z. Lv, H. Li, C. Ge, X. Zhang and T. Ma, *ACS Appl. Mater. Interfaces*, 2025, **17**, 38050–38061.

42 H. Yin, Y. Peng and J. Li, *Environ. Sci. Technol.*, 2023, **57**, 3134–3144.

43 Y. Wang, W. Zhou, R. Jia, Yifu Yu and B. Zhang, *Angew. Chemie - Int. Ed.*, 2020, **59**, 5350–5354.

44 P. Liu, J. Yan, H. Huang and W. Song, *Chem. Eng. J.*, 2023, **466**, 143134.

45 S. Zhang, M. Li, J. Li, Q. Song and X. Liu, *Proc. Natl. Acad. Sci. U. S. A.*, 2022, **119**, e2115504119.

46 J. Yang, H. Qi, A. Li, X. Liu, X. Yang, S. Zhang, Q. Zhao, Q. Jiang, Y. Su, L. Zhang, J. F. Li, Z. Q. Tian, W. Liu, A. Wang and T. Zhang, *J. Am. Chem. Soc.*, 2022, **144**, 12062–12071.

47 K. Liu, Z. Sun, X. Peng, X. Liu, X. Zhang, B. Zhou, K. Yu, Z. Chen, Q. Zhou, F. Zhang, Y. Wang, X. Gao, W. Chen and P. Chen, *Nat. Commun.*, 2025, **16**, 2167.

48 X. Ouyang, W. Qiao, Y. Yang, B. Xi, Y. Yu, Y. Wu, J. Fang, P. Li and S. Xiong, *Angew. Chemie - Int. Ed.*, 2025, **64**, e202422585.

49 L. Sun, H. Yao, F. Jia, Y. Wang and B. Liu, *Adv. Energy Mater.*, 2023, **13**, 2302274.

50 P. Wang, P. Li, Z. Pan, K. Liu, M. Xie, L. Zhou, M. Zhou, G. Yu and Z. Jin, *Nat. Commun.*, 2025, **16**, 5581.

51 M. Yi, P. Wang, R. Shi, W. Guo, D. Yang, P. Li, G. Yu and Z. Jin, *Angew. Chemie*, 2026, **138**, e21345.